# Planar microlenses for near infrared CMOS image sensors

*L. Dilhan* [1,2], *J. Vaillant* [2], *A. Ostrovsky* [1], *L. Masarotto* [2], *C. Pichard* [2], *R. Paquet* [2];

[1] *STMicroelectronics; 850 rue Jean Monnet, F-38920 Crolles; France*

[2] *Univ. Grenoble Alpes, CEA, LETI; F38000 Grenoble; France*

## Abstract

*In this paper we present planar microlenses designed to improve the sensitivity of SPAD pixels. We designed diffractive and metasurface planar microlens structures based on rigorous optical simulations. The current melted microlens solution and designed diffractive microlens were implemented on STMicroelectronics 40nm CMOS testchips (32 × 32 SPAD array), and average gains of 1.9 and 1.4 in sensitivity respectively were measured, compared to a SPAD without microlens.*

## Introduction

Our work centers on designing a wafer level planar microlens for applications in near-infrared, on Single Photon Avalanche Diode (SPAD). The current solution, which is the melted microlens [1], and two new types of planar microlenses will be compared to a SPAD without microlens to assess the average gain of all the microlenses. Optical simulations are performed using a FDTD-solutions software [2].

### SPAD macropixel

Single photon avalanche diode arrays are used in applications requiring photon counting over time, with accuracy around hundreds of picoseconds or less. The applications are set with active illumation with monochromatic wavelength of either 850, 905 or 940 nm, the latter being the most critical, being the least absorbed wavelength by the photo-sensitive area of the pixel.
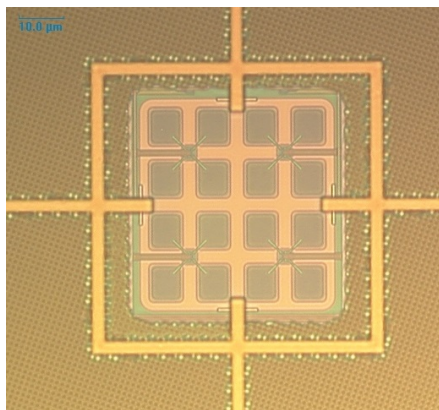


Figure 1: STMicroelectronics 40nm CMOS SPAD macropixel

One SPAD layout is considered in this work, on Front-Side Illumination (FSI) STMicroelectronics 40 nm CMOS technology, with a 11 μm pixel pitch [3]. The macropixels, see Fig. 1, are designed to share the diode N-well between 4 × 4 SPAD, allowing the pixels to have a fill-factor of ∼ 40% [4]. Light entering the upper layer of a SPAD pixel has to go through 5.4 μm of Back-End of Line stack thickness before reaching the photo-sensitive

area. It encounters metal layers on its path, being reflected and scattered in all directions before reaching the absorbing silicon layer.

### Current process: melted microlens

We want to design a microlens that focuses the light inside the SPAD pixel, to avoid the Back-End of Line metal layers in the stack and enhance the fill-factor. This microlens is deposited by photo-lithography, then melted to reach the desired dome-shape [5].

Given the symmetry of the macropixel, see Fig. 1, we simulate only a quarter of the macropixel. Fig. 2 represents a vertical cross section of the simulated pixels with the melted microlens. The colorbar indicates the index of refraction of the medium. The red bottom layer is silicon (Si), containing the photo-sensitive part of the pixel where we want to concentrate light, and the top blue layer is the entry medium, air. The dark blue represents the metal layers of the Back-End of Line.

The melted microlens has a thickness of 4 μm over the pixel, with a varying topography along the x and y axis.
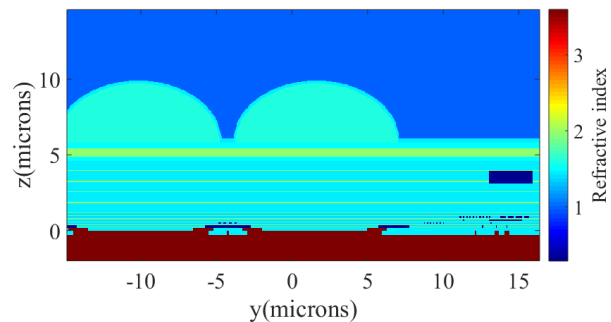


Figure 2: 2 SPAD pixels index cross-section, with melted microlens implemented

### Towards planar microlenses

A planar microlens has the advantage of being processed with common lithography-etch steps, with a shape defined by design and not through process adjustments, allowing dedicated design per pixel.

We start by investigating a diffractive planar solution, commonly refered to as Fresnel Zone Plate (FZP) microlens, conventionally used as a concentrative X-ray lens [6] [7] but also on SPAD arrays [8] [9] [10]. Then we explore the metasurfaces [11], finding a way to apply them to our application.

We present the theory behind each planar microlens, then the simulations results and finally the characterization results for all but metasurface microlens, as its development process is undergoing.

## Theory

We use two approaches to find a good suited planar microlens. Firstly, we consider the known FZP microlens [7] [10] and adapt it to our needs. Secondly, we investigate the use of a metasurface as a microlens [12].

### FZP microlens

The FZP microlens is based on the principle of diffraction, designed to focus light by constructive interferences in focus spots determined by the geometry of the microlens. The intensity is highest in the first order of diffraction, and other orders are negligible. In Fig. 3, a theoretical FZP principle schematic, we see the entry material, serving as an anti-reflective (AR) coating, with a refractive index $n_{AR}$, encapsulating the FZP microlens, with a material of index $n_{FZP}$. The FZP lens lies on an output material of index $n$.
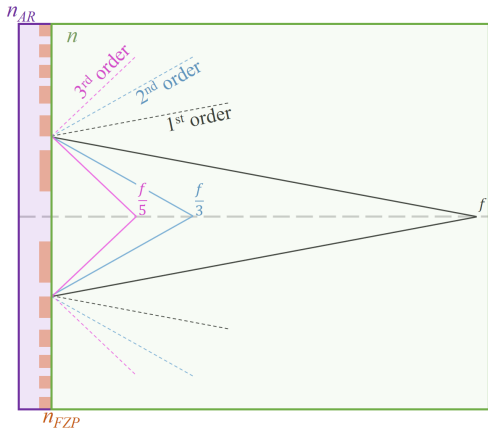


Figure 3: FZP lens diffraction principle

The conventional FZP lens is composed of concentric diffracting rings, with given inner and outer radii for each ring. The k-th radius of the rings is defined as follows:

$$r_k = \sqrt{\frac{k\lambda}{n}\left(f + \frac{k\lambda}{4n}\right)} \qquad (1)$$

Where $k$ the radius number, $f$ the focal length of the FZP microlens, $\lambda$ the working wavelength and $n$ the index of refraction of the output material, a design of FZP microlens resulting from equation 1 is shown in Fig. 4.



5 μm
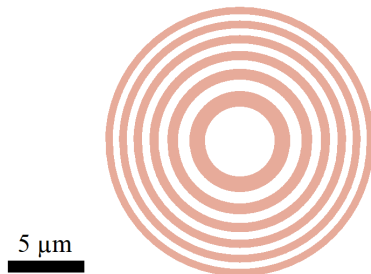
Figure 4: FZP microlens example design

In a regular amplitude FZP lens the diffracting material is an absorbant material, often metal. Here we want to maximise the transmission of the FZP microlens, we design a phase FZP where the diffracting material is chosen to specifically introduce

a $\pi$ phase shift. We control the phase shift by controlling the material's thickness $h$. In our study, we chose amorphous silicon (a:Si) as the phase-shifting material, and silicon oxide as an anti-reflective coating because they yield a high refractive index contrast. The thickness $h$ is given by:

$$h = \frac{(2m+1)\lambda}{2(n_{a:Si} - n_{AR})} \qquad (2)$$

Here $m$ is an integer giving the different thicknesses for which the inferences are constructive between the light going through the high index material and the light going through the AR material. $n_{a:Si}$ is the refractive index of amorphous silicon and $n_{AR}$ is the refractive index of the other material, anti-reflective coating or air. $m$ is chosen by considering process capability, here we used the thinnest solution ($m = 0$).

### Metasurface

Nanopillars of high refractive index with dimensions largely inferior to the working wavelength can be designed to be phase shifters [11]. We create a library of cylindrical nanopillars by simulating them with infinite periodic boundaries with given height, radius, material, pitch, wavelength and illumination incidence. Each simulation yields a result of phase shift for a particular set of parameters. We then use the information to set our desired array of nanopillars to form a metasurface, assuming that the nanopillars yield the same phase in a periodic array of similar pillars than surrounded by nanopillars with different set of parameters. It is necessary, when constructing the library, to create a set of nanopillars covering a $2\pi$ phase shift.

In our case, we design a metasurface so that the light is focused at a desired focal length, creating a metamicrolens. We use equation 3 to describe the phase-shift $\phi$ induced by an infinite plano-convex perfect lens, with a given focal length $f$ [12].

$$\phi(r) = \left[\frac{2\pi}{\lambda}\left(\sqrt{r^2 + f^2} - f\right)\right] mod(2\pi) \qquad (3)$$

We match the nanopillars from the library to the dashed line of the phase profile shown in Fig. 5, ergo designing a metamicrolens. When choosing the nanopillars from the library, we select them to have the highest possible transmission, in order to lose as little signal as possible.
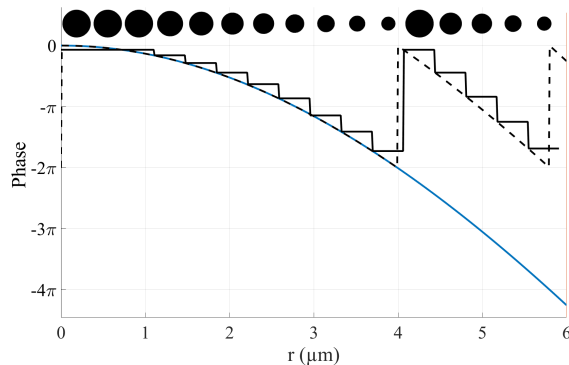


Figure 5: Infinite plano-convex lens phase profile given by eq. 3, with and without the $2\pi$ modulus, with corresponding nanopillars and their phase

In Fig. 5 are represented the nanopillars selected from the library to match the phase profile shown below. The whole metamicrolens is formed with nanopillars of different diameters, and then simulated on SPAD pixels with FDTD-solutions software [2].

## Simulations

In this part, we simulate the propagation of light [13] through the microlens into the pixels. We compare it to the reference, the pixel without microlens. In our study, we work with a plane wave with $\lambda = 940 \pm 5$ nm, and in all simulations we use the same $2 \times 2$ SPAD design and parameters, changing only the microlens from one simulation to the other. Our metrics are the percentage of absorbed light in the depleted region of the pixel, and the average optical gain comparing the absorption with and without microlens.

### No microlens, reference

Knowing the architecture of a $4 \times 4$ SPAD design, a reference simulation is done without microlens.
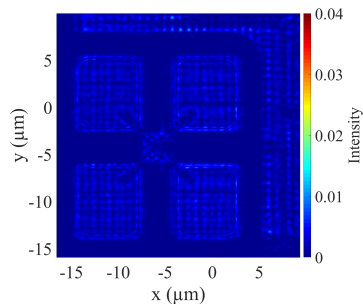


Figure 6: Light intensity at photo-sensitive area entry, no microlens

Fig. 6 represents the light intensity at the plane of entry of the photo-sensitive area. We see the imprint of the metal layers in the intensity distribution, and see that light is lost over areas that are not photo-sensitive. This is explained by the fact that light encounters several metal layers before reaching the photo-sensitive area, being scattered along its path.

### Melted microlens

We make a 3D FIB-SEM characterization of the surface of a melted microlens produced at STMicroelectronics, and simulate it with the software to have a simulation as close to reality as possible.
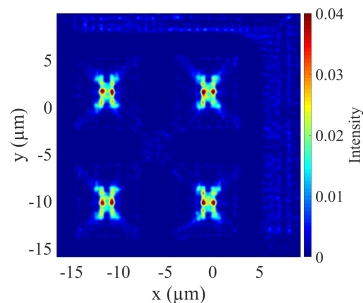


Figure 7: Light intensity at photo-sensitive area entry, melted microlens

Comparing Fig. 7 and Fig. 6, we see that here the light is focused in the center of the photo-sensitive area, increasing the

absorption of the pixel. We have a focus-spot of diameter $1.5 \pm 0.7$ μm, with an average gain of 1.5 with regard to the reference without microlens.

### FZP microlens

We put the FZP microlens on a pedestal of index $n = 1.45$, see equation 1, and thickness $\sim 2$ μm to allow some supplementary converging distance for the incoming light, avoiding the Back-End of Line metal layers. The variables of the simulations are the focal length $f$, the pedestal thickness and $h$ the thickness of the FZP microlens.

Modifying $f$ has an impact on the radii of the rings hence on the design of the FZP microlens, whereas modifying $h$ has a consequence on the etching process steps of the FZP microlens layer.

We optimize these parameters and the FZP microlens design to have the highest possible absorption in the bottom photo-sensitive layer. We use $h = 200$ nm with a AR SiO2 coating of 150 nm and $f = 8$ μm.
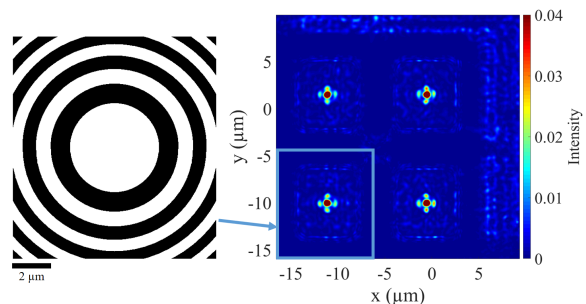


Figure 8: Top view of FZP microlens and light intensity at photo-sensitive area entry simulation result

With our design, we see in Fig. 8 that light is tightly focused at the surface of the photo-sensitive layer. We have a focus-spot with a diameter of $0.6 \pm 0.3$ μm, and an average gain of 1.2 compared to the simulation without microlens.

### Metamicrolens

After building the library of nanopillars composed of high refractive index a:Si nanopillars in SiO2 medium, we simulate a metamicrolens with the same focal length, $f = 8$ μm, as the FZP microlens to have comparable results. We select a:Si and SiO2 to have a high refractive index contrast and these two materials can be processed in the STMicroelectronics and CEA Leti cleanrooms. For this simulation, we use a pitch of 370 nm between two pillars. As with the melted and FZP microlenses, we see that the metamicrolens focuses light at the photo-sensitive layer's surface.
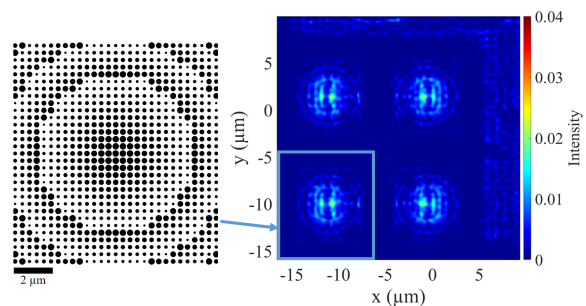


Figure 9: Top view of metamicrolens and light intensity at photo-sensitive area entry simulation result

The designed metamicrolens has a central focus-spot with a diameter of $1.0 \pm 0.6$ μm. With our design, we see an average gain of 1.8 compared to the simulation without microlens, which is better than the FZP microlens result, as the $0 - 2\pi$ phase shift is better sampled with the metamicrolens. It is also better than the melted microlens gain, as the surface covered by the metamicrolens is larger.

### *Simulation results*

In Table 1 are the simulated photon detection efficiency (PDE) with dispersion error and average gain in the photosensitive area, given for four SPAD pixels with two different polarization of the illumination. We expect to find similar results with the characterization measurements performed on the SPAD pixel without microlens, with melted microlens and with FZP microlens. The metasurface process is under developpement consequently the metamicrolens has not yet been fabricated.

Table 1: Expected average absorption and gain results

| Configuration | Simulated PDE (%) | Average gain |
|---|---|---|
| No lens | $2.2 \pm 0.2$ | – |
| Melted microlens | $3.4 \pm 0.2$ | 1.5 |
| FZP microlens | $2.6 \pm 0.1$ | 1.2 |
| Metamicrolens | $4.1 \pm 0.1$ | 1.8 |

These results are promising as all microlenses yield gain. As expected, the FZP has a low gain, as its phase is only binarized. The metamicrolens has an average gain superior to the melted microlens, we can suppose that its performances will exceed all the microlenses, once the process is developped.

## Characterization

In this part, we fabricate and characterize $4 \times 4$ SPAD pixels without microlens, with the current solution of melted microlens and with the FZP microlens. The metamicrolens is not characterized as the fabrication process is yet to be finalized. On Fig.10 are shown top views of the melted and FZP microlens, left and right respectively, after fabrication.
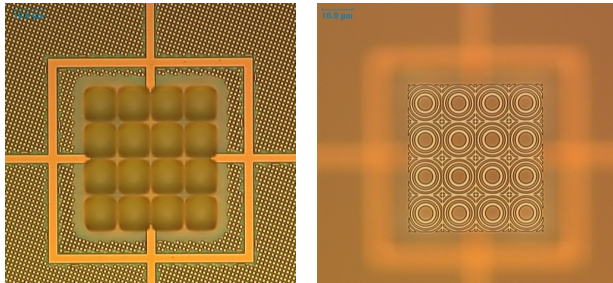


Figure 10: INS3000 microscope top view image of SPAD macropixel with left: melted microlens, right: FZP microlens

We perform Light Count Rate (LCR) and Dark Count Rate (DCR) measurements at wafer level. For LCR measurements we use a uniform narrow bandwidth illumination $\lambda = 940 \pm 5$ nm, at an $f/2$ aperture.

From these measurements, we compute the photon detection efficiency (PDE) for each pixel. The PDE is given as the number of electrons generated over the number of photons received, see equation 4.

$$PDE(\%) = \frac{N_{e^-}}{N_{photons}} \cdot 100 \qquad (4)$$

Where the number of electrons generated $N_{e^-}$ is given as the substraction of the dark count rate to the light count rate, and the number of photons $N_{photons}$ is the energy of the illumination source times the integration time over the energy of one photon. This yields equation 5.

$$PDE = \frac{(LCR - DCR).h.c}{T_{int}.I.S.\lambda} \cdot 100 \qquad (5)$$

With $h$ Planck's constant, $c$ the speed of light, $\lambda$ the wavelength of illumination, $I$ the irradiance of the source, $S$ the surface of the pixel and $T_{int}$ the integration time.

The PDE of each pixel is computed for all configurations, and represented in Fig. 11 as the statistical distribution of PDE. The data is sorted by configuration type: no microlens, melted microlens and FZP microlens. The mean PDE value of each configuration is represented by a vertical colored line.
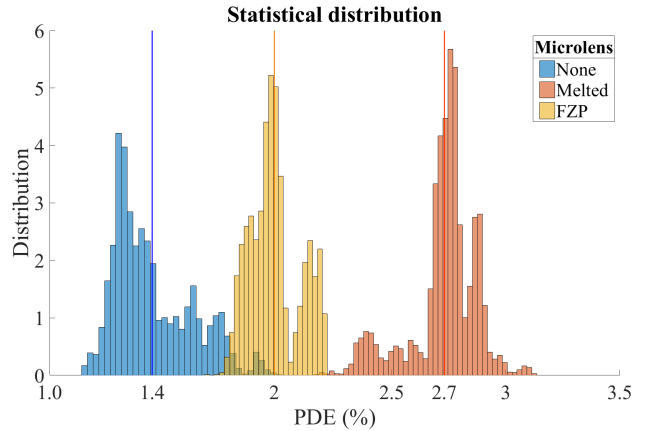


Figure 11: Statistical distribution of PDE, sorted by microlens type

From the average PDE of the measured pixels we compute the average gain of each microlens. The gain is calculated as the average PDE of a given microlens over the average PDE without microlens. The characterization measurements are resumed in the table below (Tab. 2).

Table 2: Characterization measurements, PDE mean value and dispersion and average gain per microlens type

| Configuration | PDE (%) | Average gain |
|---|---|---|
| No lens | $1.4 \pm 0.2$ | – |
| Melted microlens | $2.7 \pm 0.1$ | 1.9 |
| FZP microlens | $2.0 \pm 0.1$ | 1.4 |

### Analysis

On Fig. 11 for the FZP microlens, we see two different populations. One group with a PDE around 1.9 %, and another smaller group around 2.1%. The smaller group probably encloses the four central pixels of a macropixel. There presumably is optical or electronic cross-talk between pixels, and the central pixels generate more electrons than their surrounding neighbors, hence their PDE is higher than their surrounding neighbors.

Given that the illumination parameters are different between simulation and characterization, we compare relatively the average gain column of Tables 1 and 2.

The melted microlens characterization is higher than the simulation probably due to the simulations approximations when replicating the processed melted microlens. Only one melted microlens has been characterized through 3D FIB-SEM to be simulated, meaning that the simulations of the melted microlens are dependent on the quality of this characterized microlens. Approximations are also made on the layer coating the melted microlenses. Its thickness over the resist is not completely characterized.

Characterization measurements, as the simulations, show the FZP microlens is less efficient than the melted and metamicrolens. This is probably due to the poor binary 0 and $\pi$ phase sampling of the FZP microlens.

We expect the metamicrolens to be slightly better than the melted microlens as their fill-factor differ a bit. There is a gap between melted microlens that is non-existent with the metamicrolens, consequently the metamicrolens has a slightly greater fill-factor than the melted microlens. The metamicrolens has a better phase sampling than the FZP microlens, hence its PDE should be higher.

### Conclusion

In this study, we have demonstrated the capability to improve SPAD sensitivity by using different types of microlenses in the near infrared. Considering Fresnel Zone Plate and metasurface structures, we designed microlenses based on rigorous optical simulations taking into account the SPAD layout, the CMOS technology and the current microlens solution. The current microlens solution and Fresnel Zone Plate microlens were implemented on STMicroelectronics 40nm CMOS testchips and gains of 1.9 and 1.4 in sensitivity respectively were measured compared to a SPAD without microlens. The technologies described in this paper offer several advantages like planarization, simplicity in design and process or the capability to focus light.

### Acknowledgments

### References

[1] G. Intermite et al, Enhancing the Fill-Factor of CMOS SPAD Arrays Using Microlens Integration, Proceedings of SPIE, Vol. 9504 (2015).

[2] High-Performance Nanophotonic Simulation Software, http://www.lumerical.com/.

[3] S. Pellegrini et al, Industrialised SPAD in 40 Nm Technology, 2017 IEEE International Electron Devices Meeting (IEDM), pp. 16.5.1-16.5.4 (2017).

[4] S. Pellegrini, International SPAD sensor workshop (2018).

[5] Y.-T. Fan, C.-S. Peng, et C.-Y. Chu, Advanced microlens and color filter process technology for the high-efficiency CMOS and CCD image sensors, vol. 4115, p. 263-274 (2000).

[6] A. G. Michette, Optical Systems for Soft X-Rays, Plenum, London (1986).

[7] Max Born et al, Principles of Optics: Electromagnetic Theory of Propagation, Interference and Diffraction of Light, 7th ed. Cambridge University Press (1999).

[8] F. Hirigoyen, Fresnel Zone Plates : plasmonics filtering for SPADS sensors, International Image Sensor Workshop (IISW), P45 (2017).

[9] Sheng-Chuan Cheng et al, Lens Solution for Intensity Enhancement in Large-Pixel Single-Photon Avalanche Diode, International Image Sensor Workshop (IISW), R17 (2017).

[10] J. Vaillant et al, SPAD array sensitivity improvement by diffractive microlens, International Image Sensor Workshop (IISW), P28 (2019).

[11] Lalanne, P., Chavel, P., Laser & Photonics Reviews, 11, 1600295 (2017).

[12] Yu, N. & Capasso, F., Flat optics with designer metasurfaces, Nature Materials, Nature Publishing Group, a division of Macmillan Publishers Limited. All Rights Reserved., 13, 139 (2014).

[13] A. Crocherie et al, Three-Dimensional Broadband FDTD Optical Simulations of CMOS Image Sensor, vol. 7100, 71002J-71002J-12 (2008).

## Author Biography

*Lucie Dilhan received her M. Sc. in Optical Physics from Institut d'Optique Graduate School in Palaiseau, France (2017) and her M. Sc. in Biomedical Physics from the Royal Institute of Technology in Stockholm, Sweden (2018). Since then she is pursuing with a PhD conducted between STMicroelectronics R&D center in Crolles, France, and CEA in Grenoble, France. Her work is focused on the development of planar microlenses for imager applications.*

*Jérôme Vaillant received his M. Sc. in Optical Engineering from Ecole Centrale de Marseille, France (1996), his M. Sc. Degree in Astrophysics from Grenoble Alps University, France (1997) and his Ph.D. in Astrophysics from Lyon University, France, in 2000. Since then he has worked on CMOS image sensor with a focus on optics at pixel. Starting in 2000 at STMicroelectronics R&D center in Crolles, France, he joined CEA in Grenoble, France, in 2012.*

*Alain Ostrovsky received the M. Sc. in Opto-electronics and Micro-electronics from Ecole Nationale Supérieure d'Ingénieurs, Caen ISMRa, in 1994. He joined the Thin film group of Jobin Yvon company in the US for 5 years concentrating on ellipsometry and optical endpoint for micro-electronic industry. He joined STMicroelectronics Crolles in 2000 to develop integrated metrology solutions, since 2008 he works as lithography process engineer developing R&D CMOS digital and CMOS image sensor technologies.*

*Lilian Masarotto received his M. Sc. in Material Sciences from Institut National des Sciences Appliquées, Toulouse, France (1998) and his Ph.D. in Integrated Electronic devices from Institut National des*

*Sciences Appliquées, Lyon, France, in 2001. In 2002, he joined CEA-Leti in Grenoble and worked on developing high thermal deposition processes of thin layers and nanocrystals by RPCVD or vertical LPCVD tools. Since 2011, he has worked on the development of integrated optical structures on CMOS image sensors.*

*Céline Pichard received her BTEC National Diploma in Thermal Engineering and Energy from Joseph Fourier University in Grenoble, France (2001). Since then she has worked on production process, starting in 2001 at STMicroelectronics R&D center in Crolles, France, she joined CEA in Grenoble, France, in 2018.*

*Romain Paquet was born in 1990. He received the Master degree in optoelectronics and microwave engineering in 2013 at Univ. of Montpellier. In 2016, he obtained the Ph.D. degree from Univ. of Montpellier on dual frequency lasers for THz generation. Since 2017, he joined the Atomic Energy and Alternative Energies Commission. His current research interests are CMOS image sensors and single photon avalanche photodiodes.*